Journal of Hazardous Materials 424 (2022) 127504

Contents lists available at ScienceDirect

Journal of Hazardous Materials

journal homepage: www.elsevier.com/locate/jhazmat

Research Paper

Highly efficient removal of Cr(VI) by hexapod-like pyrite nanosheet clusters

Xin Nie [a], Guiying Li [b], Yun Wang [c,*], Yingmei Luo [d], Lei Song [e], Shuguang Yang [a], Quan Wan [a,f,**]

[a] State Key Laboratory of Ore Deposit Geochemistry, Institute of Geochemistry, Chinese Academy of Sciences, Guiyang 550081, China
[b] Guangdong Key Laboratory of Environmental Catalysis and Health Risk Control, Guangzhou Key Laboratory Environmental Catalysis and Pollution Control, School of Environmental Science and Engineering, Institute of Environmental Health and Pollution Control, Guangdong University of Technology, Guangzhou 510006, China
[c] Centre for Catalysis and Clean Energy, School of Environment and Science, Gold Coast Campus, Griffith University, Gold Coast, QLD 4222, Australia
[d] School of Chemistry and Materials Science, Guizhou Normal University, Guiyang 550001, China
[e] School of Chemistry and Materials Science, Guizhou Education University, 115 Gaoxin Road, Wudang District, Guiyang 550018, Guizhou, China
[f] CAS Center for Excellence in Comparative Planetology, Hefei 230026, China

ARTICLE INFO

Editor: Dr. L. Haizhou

Keywords:
Pyrite
Hexapod-like nanosheet clusters
Hexavalent chromium
Adsorption
Reduction

ABSTRACT

Pyrite nanomaterials show an excellent performance in remediating Cr(VI) contaminated wastewater. However, the high surface reactivity makes them easy to agglomerate to reduce their removal efficiency for Cr(VI). In this study, a novel hexapod-like pyrite nanosheet clusters material was successfully synthesized via a facile hydrothermal method with the assistance of fluorides. The products were pyrite microspherulites without fluoride ion. The hexapod-like pyrite nanosheet clusters had dramatically higher Cr(VI) removal efficiencies than microspherulites due to more dissolved Fe(II) and S(-II) into the suspension released for nanosheet clusters should be responsible for the enhanced removal rate of Cr(VI). The XPS analysis revealed that the rapid adsorption on the surface of pyrite nanosheet clusters followed by reduction of Cr(VI) to Cr(III) by FeS_2 and subsequent precipitation of Cr(III) hydroxides/oxyhydroxides are responsible for the high removal capacity of Cr(VI). The hexapod-like pyrite nanosheet clusters material had high stability and longevity, and did not aggregate during the Cr(VI) removal process. The removal efficiency of Cr(VI) was still 100% after 5 cycles. Our study shows that the hexapod-like pyrite nanosheet clusters material could be acted as a recyclable and promising mineral material with high activity, stability, feasibility for remediating Cr(VI) contaminated environment.

1. Introduction

As a common geochemical element, chromium (Cr) is widely distributed in rocks, minerals soils, water and atmosphere. Cr has been extensively applied in steel, plastics, inks, paints, and leather tanneries (Yasir et al., 2021). The transport, fate, and bioavailability of Cr in water and soil environment is mainly controlled by the valence state of Cr. Hexavalent Cr (Cr(VI)) and trivalent Cr (Cr(III)) are the most stable and dominant species of Cr in the natural environment. The migration, toxicity, bioavailability, and persistence of Cr(VI) is significantly higher than Cr(III), which is less mobile, nontoxic, relatively inert, and an essential dietary element for human (Xia et al., 2019; Shahid et al., 2017; Veerakumar and Lin, 2020). As a notorious heavy metal ion pollutant with highly acute toxicity, non-biodegradability, carcinogenic, teratogenic and mutagenic effects to living organisms, Cr(VI) has normally been found in soil and various aquatic environments originating from both natural processes and the increasing anthropogenic activities, such as agricultural, industrial, and mining production (Xia et al., 2019; Veerakumar and Lin, 2020; Farooqi et al., 2021; Stern et al., 2021). The presence of excessive amounts of Cr(VI) poses a highly health and environmental risk on human and ecosystem due to its accumulation and amplification effect through food chains (Azeez et al., 2021). Therefore, highly efficient removal technologies for Cr(VI) are imperative.

Considerable efforts have been made to eliminate toxic Cr(VI) contaminated soils and wastewater via reducing its total concentrations, migration capacity and bioavailability. Various treatment techniques, include adsorption, membrane filtration, ion-exchange, chemical reduction and precipitation, electrochemical process, bioremediation, and advanced oxidation/reduction process, have been employed for eliminating Cr(VI) contamination (Xia et al., 2019; Farooqi et al., 2021; Stern et al., 2021; Azeez et al., 2021; Wen et al., 2018; Marinho et al.,

* Corresponding author.
** Corresponding author at: State Key Laboratory of Ore Deposit Geochemistry, Institute of Geochemistry, Chinese Academy of Sciences, Guiyang 550081, China.
E-mail addresses: yun.wang@griffith.edu.au (Y. Wang), wanquan@vip.gyig.ac.cn (Q. Wan).

https://doi.org/10.1016/j.jhazmat.2021.127504
Received 17 August 2021; Received in revised form 28 September 2021; Accepted 11 October 2021
Available online 14 October 2021

2019; Fernandez et al., 2018; Xu et al., 2019; Gong et al., 2018). Despite extensive efforts and significant progress have been made, the practical application of most treatment techniques for Cr(VI) removal were still limited due to the potential secondary pollution, high cost, time consuming, and the unsatisfactory removal efficiency (Azeez et al., 2021). Among these techniques, adsorption stands out due to its simplicity, high removal efficiency, and low cost. However, multistep preparation of adsorbent and incomplete removal of Cr(VI) are main limitations of adsorption technology (Farooqi et al., 2021; Sahu et al., 2021b, 2020, 2021a; Ekka et al., 2021; Tripathy et al., 2021). To overcome these drawbacks, simultaneous adsorption and reduction-based method is proposed to be an effective strategy for the elimination of Cr(VI) contaminants due to its environmentally friendly nature and reusability.

Owing to the higher efficiency, nontoxicity, inexpensiveness, and high reactivity, iron-bearing reducing nanomaterials including magnetic iron oxide, ferrous sulfides (such as mackinawite FeS, pyrite FeS_2), zero-valent iron (ZVI), and their derivatives, have been reported to be as adsorbents as well as effective reductants to convert highly soluble and toxic Cr(VI) to non-toxic and immobile Cr(III) solids and have attracted huge attention (Shao et al., 2018; Gong et al., 2016; He et al., 2021; Wang et al., 2019a, 2019b; Liu et al., 2019). However, magnetic iron oxide and zero-valent iron nanoparticles are highly prone to aggregation during Cr(VI) removal process, which results in loss of their activity and cannot be recycled easily (Farooqi et al., 2021). Pyrite nanomaterials have fetched considerable attention because they do not only provide a higher surface area for adsorption of Cr(VI) but also the simultaneously containing Fe(II) and S(-I) species are effective reductants for reducing sorbed Cr(VI) as well as aqueous Cr(VI) to less toxic Cr(III). Cr(III) would be precipitated subsequently in the form of their hydroxides in solid phase, which have low negative effect on environment (Wang et al., 2019b; Yang et al., 2021; Demoisson et al., 2005, 2007; Li et al., 2016a, 2016b; Kirkeminde and Ren, 2013). However, the high surface reactivity also makes pyrite nanomaterials easy to agglomerate, which would decrease the removal efficiency of Cr(VI) (Farooqi et al., 2021). To overcome this drawback, it is necessary to find a suitable nanostructured pyrite with superior performance and high stability. Recently, two-dimensional pyrite nanosheets have been demonstrated to have excellent adsorption capacity for toxic Cr(VI) (Farooqi et al., 2021). Consequently, they are highly promising for the Cr(VI) removal from wastewater and soil.

Abovementioned excellent physicochemical properties and promising applications of pyrite nanosheets have motivated considerable efforts that have aggressively targeted their synthesis by various routes, including hydrothermal/solvothermal, hot injection, heating-up, sulphidation, and liquid-phase exfoliation methods using different chemical precursors (Khalid et al., 2018; Caban-Acevedo et al., 2013; Xian et al., 2016; Kirkeminde et al., 2012; Hu et al., 2008; Wu et al., 2020; Kaur et al., 2020). Hydrothermal method is the most promising and scalable method due to its simplicity, low cost, and moderate reaction conditions. The surface physicochemical properties, geometrical morphologies and sizes of pyrite nanosheets could be tuned by employing capping agents or morphology-controlling agents, which can selectively adsorb on specific facets of crystal seeds to reduce the total surface energy of the adsorbed facets and modify the crystal growth along specific direction accordingly, and consequently constructing the shape of the final crystals (Khalid et al., 2018; Liu et al., 2011; Wang et al., 2019c; Bai et al., 2013). However, the capping agents or morphology-controlling agents are usually organics, which would affect the surface reactivity of pyrite nanosheets and must be eventually removed to obtain clean facets (Zhu et al., 2012). This may further lead to some uncontrollable variations of surface atomic structures and unavoidably influence the surface physicochemical properties (Liu et al., 2011). Therefore, a reliable method to facilely synthesize uniform and phase pure pyrite nanosheets with controllable morphology, high activity, stability as well as longevity remains a significant challenge and still needs to be further developed. Recently, we reported a novel hexapod-like pyrite nanosheet clusters material for highly efficient adsorption and degradation of refractory organic pollutants of ciprofloxacin (Nie et al., 2022). However, the use of the hexapod-like pyrite nanosheet clusters material as a recyclable material with high stability and excellent performance for Cr (VI) removal by adsorption combined with in-situ chemical reduction has not been explored yet.

Herein, the hexapod-like pyrite nanosheet clusters with a single morphology and uniform size were successfully synthesized using a facile hydrothermal method with fluoride ion as a capping and morphology-controlling agent. The shape of hexapod-like nanosheet clusters can effectively prevent the aggregation of particles and enhance their stability. The effects of initial solution conditions (including pH, concentrations of Cr(VI), and co-existing organic matter) on Cr(VI) removal were specifically elucidated. The stability and reusability of hexapod-like pyrite nanosheet clusters were examined. The possible mechanism for Cr(VI) removal by the hexapod-like pyrite nanosheet clusters was also proposed. Our findings could open new opportunities in the design and fabrication of other two-dimensional metal sulfides nanomaterials with enhanced performance in eliminating toxic heavy metal ion pollutant.

2. Experimental section

2.1. Synthesis and characterizations of the hexapod-like pyrite nanosheet clusters

The hexapod-like pyrite nanosheet clusters were synthesized by a hydrothermal method by using deoxygenated deionized water in all experiments (Nie et al., 2022). In a typical process, 0.015 mol of $FeSO_4{\cdot}7H_2O$ was first mixed in 20 mL of water at room temperature. Then 0.015 mol of $Na_2S{\cdot}9H_2O$ and 0.015 mol of S were dissolved into 20 mL of water and heated until the solution became transparent, which was subsequently added dropwise to the above suspension under vigorous stirring for 10 min. After that, 0.326 g NaF was added into above suspension, and the pH of suspension was adjusted to 4.0. The suspension was then transferred into 100 mL Teflon-line autoclave and kept at selected temperatures and at different intervals in an oven. After the hydrothermal reaction, the resulting black product was collected by centrifugation, and thoroughly washed with water, 1 mol/L of Na_2S boiling solution, 1 mol/L HCl, and absolute ethanol for several times. Finally, the as-synthesized sample was dried at 30 °C in a vacuum oven and then stored in an anaerobic environment.

The crystal phase composition were characterized by X-ray diffraction (XRD, Empyrean, PANalytical B.V) operating with Cu-Kα radiation. The elemental composition was characterized by X-ray photoelectron spectroscopy (XPS, Thermo Fisher K-Alpha) using monochromated Al Kα (1486.6 eV) source operated at 110 W, and the C 1s peak at 284.8 eV was used to calibrate the XPS spectra. The morphologies of the samples were observed by field emission scanning electron microscopy (FESEM, Scios, FEI Company) with an acceleration voltage of 30.0 kV and transmission electron microscope (TEM, Tecnai G2 F20 S-Twin, FEI Company, Hillsboro, OR). The specific surface area was analyzed by a nitrogen adsorption apparatus (Autosorb-iQ2-MP, Quantachrome). The N_2 adsorption data from relative pressure (P/P_0) 0.05–0.3 were obtained at 77 K (− 196 °C). The specific surface areas of the samples were calculated by multi-point BET (Brunauer-Emmett-Teller) method. The zeta potentials and the hydrodynamic diameters of samples were measured with electrophoretic effect using a multi angle particle size and high sensitive zeta potential analyzer (Omni, Brookhaven, USA).

2.2. Cr(VI) Removal experiments

The reaction solution was stirred by using a magnetic stirrer throughout the experiment. In a typical adsorption experiment, 0.1 g of pyrite was added into 100 mL solution containing 20 mg/L Cr(VI)

(potassium dichromate). At different time intervals, suspension samples were collected and filtered through a 0.45 mm Millipore filter for the late analysis. A series of parameters including initial pH (3.0–11.0) and temperatures (25–60 °C) on the Cr(VI) removal were systematically tested. The concentration of Cr(VI) in the solution was determined by UV–VIS spectrophotometry (Agilent, Cary 300) at the wavelength of 540 nm following the 1,5-diphenylcarbazide method after the solution was diluted 10 times (Balasubramanian and Pugalenthi, 1999). Total chromium (Cr(VI) and Cr(III), Cr_{total}) concentration in aqueous solution was measured with a Inductively Coupled Plasma Mass Spectrometry (ICP-MS, NexION 300x, PerkinElmer) after the solution was diluted 20 times. The concentration of Cr(III) was calculated via the difference between the Cr_{total} and Cr(VI) concentrations. Dissolved Fe(II) concentration was tested by the 1,10-phenanthrolin method with a UV–VIS spectrophotometry at a specific wavelength of 510 nm (Liu et al., 2015). The concentration of S(-II) in the solution was detected by a sulfide ion selective electrode. After reaction with Cr(VI), the suspension was collected and centrifuged for 5000 rpm. The solid specimen was dried at 30 °C in a vacuum oven, and its surface chemical species of elements was measured by XPS and visualized using a FESEM. Pseudo first order kinetic model was used to determine the removal rate constants ($k_{Cr(VI)}$) of Cr(VI) ($-dC/dt = k_{Cr(VI)}$ C) (Farooqi et al., 2021). The data showed in this study were the average values obtained from experiments replicated in triplicate.

3. Results and discussion

3.1. Structural and morphological characterizations of synthesized hexapod-like pyrite nanosheet clusters

The effect of the hydrothermal temperature on the morphological evolution of the as-synthesized samples was investigated within the temperature range of 25–220 °C. Fig. 1a shows that the diffraction peaks at $2\theta = 28.51°$, 33.08°, 37.11°, 40.78°, 47.41°, 56.28°, 59.02°, 61.69°, and 64.28° were attributed to the (111), (200), (210), (211), (220), (311), (222), (023), and (321) planes of cubic pyrite (FeS_2) (JCPDS card no. 42-1340), respectively (Nie et al., 2019). The XRD patterns of all samples exhibited similar characteristics, implying that pyrite was the only crystalline phase in all samples. The characteristic diffraction peaks were sharp and narrow, suggesting a good crystallinity of the as-synthesized samples (Nie et al., 2019). When the hydrothermal temperatures increased from 25 to 160 °C, the peak intensities of pyrite increased, implying that increasing hydrothermal temperature was beneficial to the growth of pyrite particles and the enhancement of crystallinity. While further increase of the hydrothermal temperature to 220 °C resulted in a decrease of the peak intensities of the pyrite. The surface morphologies and detailed crystal structures of as-prepared samples were characterized using FESEM and HR-TEM. When the hydrothermal temperature was ranged from 25 to 160 °C, the typical FESEM images (Fig. 2a–e) of the samples demonstrated a large quantity of orthogonal nanostructures of hexapod-like pyrite nanosheet clusters with good uniformity, in which clusters of nanosheets were oriented into a hexapod, and each pod had a length of approximately 1–3 μm. The average thickness of each nanosheet was about 10–50 nm or less. The arrangement of pyrite nanosheets was highly directional, in which nanosheets grew mainly along six orthogonal directions, implying preferential growth along specific crystallographic directions (Nie et al., 2022; Yang et al., 2013). Furthermore, it can be observed that the nanosheets were cuspate, implying that the nanosheets were initially grown as separated nanowires or needle-like nanostructures and then formed into nanosheets after lateral growth. Moreover, no remarkable morphology change can be observed with this hydrothermal temperature range. The low-magnification TEM image (Fig. 2g) of the sample synthesized at 120 °C shows the sample consisted of well-defined nanosheet-shaped structures having a width of about 50–150 nm. The HRTEM image (Fig. 2h) recorded from the yellow circled area in Fig. 2g indicates a well-crystalline nature with a clear lattice fringes spacing of ca. 0.27 nm, corresponding to (200) crystallographic interplanar distances of pyrite FeS_2 single crystals. The zone axis of this nanosheet is [001], confirming that they are terminated with {100} facets, which is the most stable surface for pyrite (Caban-Acevedo et al., 2013; Shukla et al., 2016). The two-dimensional spot array in the fast Fourier transform (FFT) pattern (Fig. 2i) of the corresponding HRTEM image with a square symmetry and the continuous lattice fringes in whole nanosheet region reveal that each pyrite nanosheet has a perfect single crystalline structure (Meng et al., 2014; Nie et al., 2022; Yu et al., 2015). The result is consistent with the cubic structure observed in XRD, providing convincing evidence that hexapod-like pyrite nanosheet clusters are formed and grew along the six equivalent <001> directions at a fast growth rate (Yang et al., 2013). When the temperature is further increased up to 220 °C (Fig. 2f), the pyrite nanosheets significantly became shorter and thicker. This might be attributed to the growth rate on the <001> direction was decreased to some extent at high temperature, leading to the decrease of the ratio between the pyrite crystal growth rates along the <001> and <111> directions (Meng et al., 2014). Furthermore, enhanced crystal nucleation rate at elevated temperature would increase the number of crystal nuclei of pyrite, resulting in pyrite nanosheets growth would cease earlier due to the exhaustion of FeS_2. Additionally, a higher dissolution rate of pyrite at the tip of the nanosheet at high temperature may also cause the nanosheet to become shorter.

For comparison, the samples synthesized in the absence of fluoride ion were also investigated at the same temperature range (25–220 °C) (Fig. 3). The solid products obtained at hydrothermal temperatures

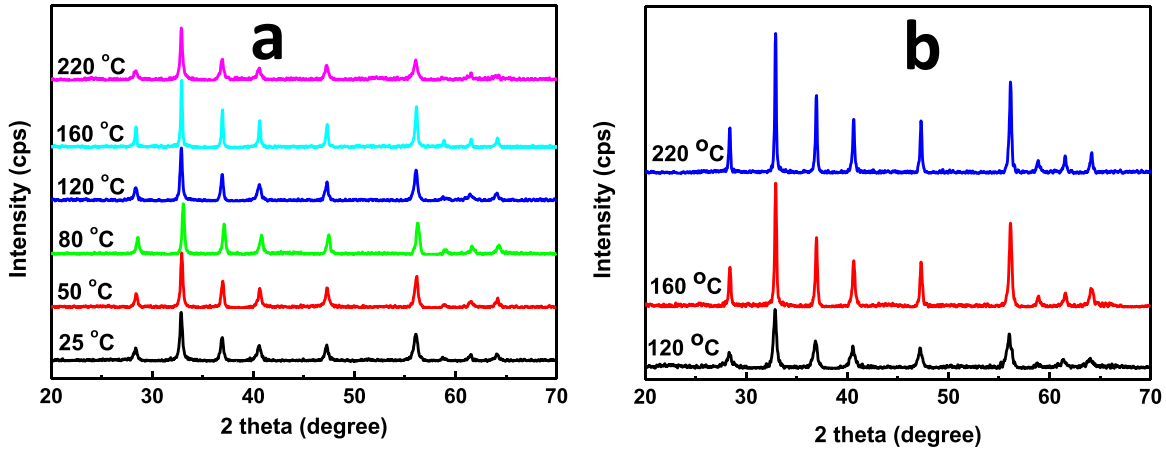

Fig. 1. XRD patterns of the pyrite synthesized at different hydrothermal temperatures for 24 h in the presence (a) and absence (b) of fluoride ion.

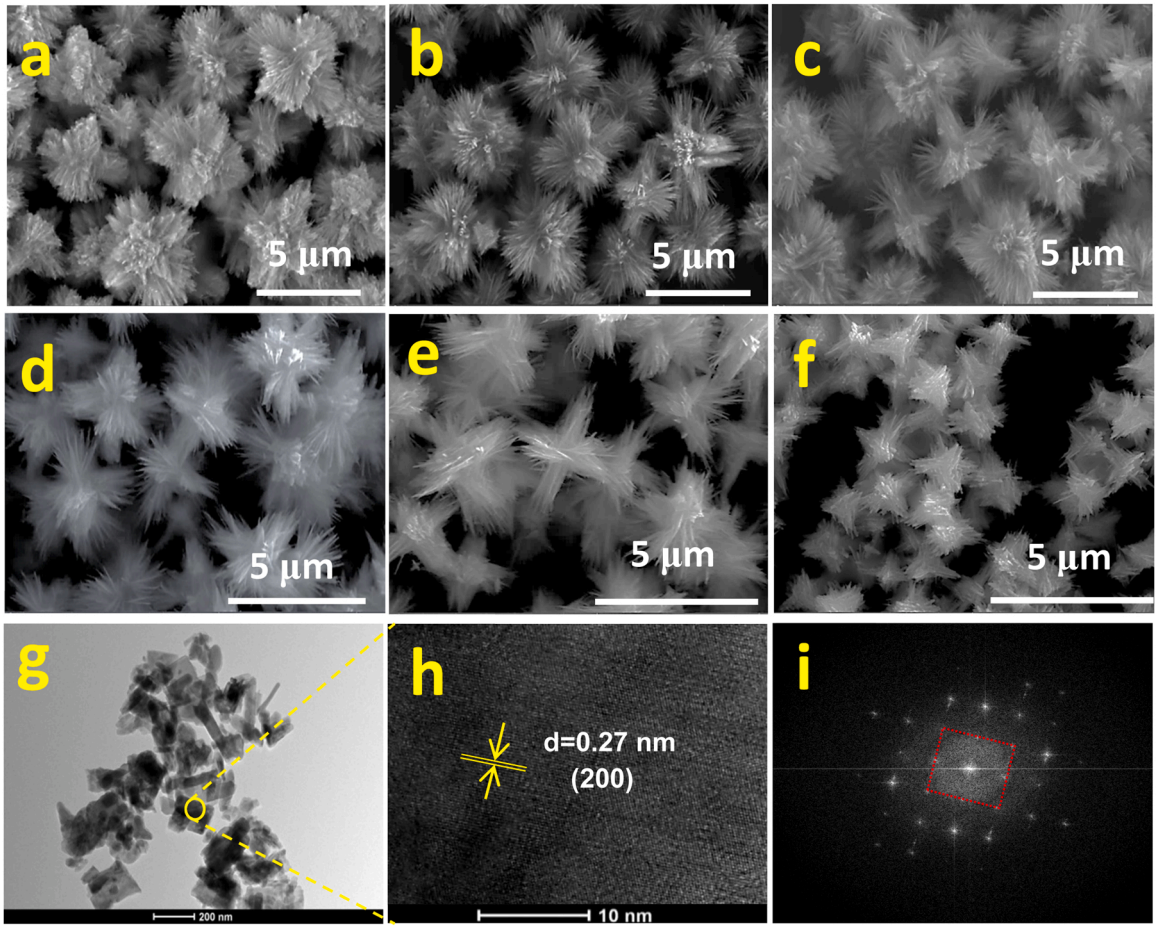

Fig. 2. FESEM images of the hexapod-like pyrite nanosheet clusters synthesized at different hydrothermal temperatures for 24 h in the presence of fluoride ion: (a) 25 °C; (b) 50 °C; (c) 80 °C; (d) 120 °C; (e) 160 °C; (f) 220 °C. Low-magnification TEM image (g), and high-magnification TEM (HRTEM) image (h) with the corresponding fast Fourier transformed (FFT) pattern (i) of lattice fringing pattern for the hexapod-like pyrite nanosheet clusters synthesized at 120 °C. (For interpretation of the references to colour in this figure, the reader is referred to the web version of this article.)

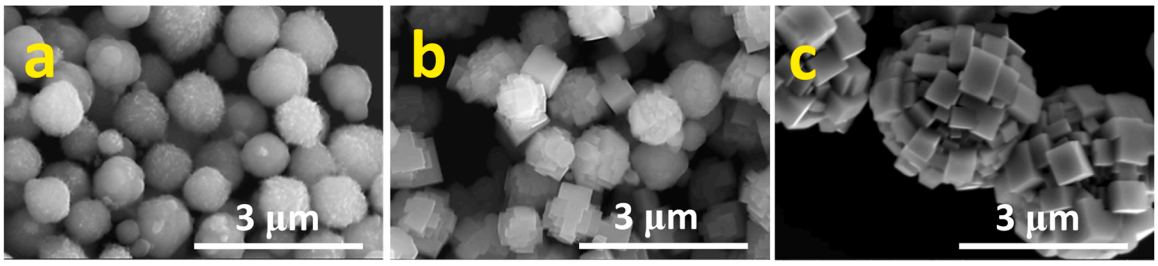

Fig. 3. FESEM images of the pyrite microspherulites synthesized at different hydrothermal temperatures for 24 h in the absence of fluoride ion: (a) 120 °C; (b) 160 °C; (c) 220 °C.

≤ 80 °C were thoroughly dissolved during the washing process, indicating that no pyrite crystal could be formed at low hydrothermal temperatures without fluoride ion. Apparently, without the addition of fluoride ion, the morphologies of the products were mainly microspherulites. The absence of nanosheets indicates that the fluoride ion is essential to the formation of nanosheet-like structures. For the sample synthesized at 120 °C, the microspherulites (~1 μm) consisted of aggregated nanoparticles with irregular spherical shape were obtained. As the hydrothermal temperature increased to 160 °C, cubic single crystals as well as microspherulites (~1 μm) composed of cubes with missing corners were observed. When the temperature was further increased up to 220 °C, the microspherulites composed of cubes were formed, and the size of microspherulites significantly increased to ~3 μm, suggesting that high hydrothermal temperature was beneficial to the nucleation, growth and aggregation of pyrite cubic crystals to form microspherulites via oriented attachment (OA) mechanism (Yu et al., 2015). This is consistent with the XRD results (Fig. 1b) that the diffraction peak intensities of pyrite increased rapidly with increasing the hydrothermal temperature from 120 to 220 °C.

To better understand the growth process and mechanism of hexapod-like pyrite nanosheet clusters, a series of experiments were performed by changing the reaction time under different temperatures, and their morphological evolution were investigated in detail (Figs. S1–S5). The required minimum reaction times for formation of pyrite at different hydrothermal temperatures with addition of fluoride ion are shown in Figs. S1. When the temperature was raised from 25° to 220 °C, the

minimum reaction times required to obtain pyrite significantly decreased from 12 h to 20 min. It indicates that the high temperature can promote the nucleation and growth rate of pyrite crystal. For the hydrothermal temperature of 120 °C, when the reaction time was 1 h (Fig. 4a), hexapod-like pyrite with octahedral morphologies but without nanosheet structures were obtained, which suggests that pyrite nucleate seeds were starting to form. The textured surfaces especially at the top of six pods represented nucleation sites for the nanosheets. When the time was ranged from 2 to 4 h, hexapod-like pyrite clusters consisting of long nanosheets could be observed. The presence of smaller ones represented that the nanosheets were in the process of growing. Further increasing the reaction times to 24 h showed a similar morphology, except the size of hexapod-like pyrite nanosheet clusters were more uniform. This confirms that the nanosheets were initially started at surface defects on top of octahedral hexapod-like pyrite nucleate seeds, and then the nanosheet clusters formed due to lateral growth along the six equivalent <001> directions (Yang et al., 2013). Additionally, the morphological and phase compositional evolution of the products prepared at different hydrothermal temperatures also showed similar tendencies with increasing reaction times (Figs. S2–S5), in which the nucleation and growth process of hexapod-like pyrite nanosheet clusters could be clearly observed. This indicates that the addition of fluoride ion could also affect both the morphology and required minimum reaction times for the formation of pyrites at all conducted hydrothermal temperatures. No hexapod-like seeds formed when fluoride ion was absent in the entire reaction duration at hydrothermal temperature of 220 °C (Figs. S6), again supporting the paramount and irreplaceable role of fluoride ion for obtaining hexapod-like pyrite nanosheet clusters. The hydrothermal temperature plays a key role in controlling the length and thickness of the pyrite nanosheets.

Based on the above results, a possible growth mechanism of hexapod-like pyrite nanosheet clusters was tentatively proposed. The fluoride ion plays a crucial role in controlling the crystal growth rate, morphology and size of the as-prepared pyrite. To obtain the hexapod-like pyrite nanosheet clusters with exposed {100} facets, sufficient fluoride ion in the solution was a prerequisite to act as a capping or shape-controlling agent. In the early stage, when the solution is supersaturated (with respect to pyrite), pyrite nucleate seeds with hexapod-like morphology formed in the presence of fluoride ion. Due to a high affinity of Fe for fluoride, which can stabilize FeS_2 via a F–Fe interaction, the preferential adsorption of fluoride ion on the surface of pyrite crystal can facilitate the faster growth rate along the six equivalent <001> direction (Li et al., 2016a 2016b; Liu et al., 2011). A large density of defects or high energy reactive sites on the surface of pod-top could act as nucleation sites and promote the adsorption of FeS_2 and subsequent crystal growth. As the reaction process proceeds, newly arriving FeS_2 adsorbed on the surface of the pods are integrated into the crystal lattice along six equivalent <001> directions. Furthermore, the acute angle existed in hexapod-like pyrite nucleate seeds would presumably show higher surface energy, simultaneously leading to a fast growth of pyrite (Liu et al., 2011). Finally, the hexapod-like pyrite nanosheet clusters with exposed {100} facets are formed via crystal continuous growth. Furthermore, high temperatures will lead to the crystal grow along the <001> as well as <111> directions. These results might provide a crucial clue to synthesize highly reactive metal sulfides materials with two-dimension nanosheet structures by selecting suitable capping agent and controlling the reaction conditions to modify the crystal growth direction (Khalid et al., 2018). Furthermore, the shape of hexapod-like nanosheet clusters could effectively prevent the aggregation of pyrite particles, and enhance their size uniformity as well as physical stability via steric effect. Based on the aforementioned analysis, it can be seen that high reaction temperature or longer reaction time (at low reaction temperature) in the presence of fluoride ion enable the formation of well-defined hexapod-like pyrite nanosheet clusters (Kirkeminde et al., 2012).

3.2. Removal of Cr(VI) by the pyrite prepared at different hydrothermal conditions

Fig. 5a shows the removal curves of Cr(VI) with an initial pH of 5.0 by the hexapod-like pyrite nanosheet clusters prepared at different hydrothermal temperatures. For the samples synthesized at 25 and 50 °C, Cr(VI) could be completely removed within 300 min, and the removal rate constants of Cr(VI) ($k_{Cr(VI)}$) increased from 0.0145 to 0.0174 min^{-1}. The Cr(VI) removal rate improved significantly and all Cr(VI) was removed within 120 min by the samples prepared at 80–160 °C, and the samples prepared at 120 °C exhibited a relatively higher Cr(VI) removal rate. Specifically, the value of $k_{Cr(VI)}$ was 0.0336, 0.0383, and 0.0352 min^{-1} for he samples prepared at 80, 120, and 160 °C, respectively. Nevertheless, further increasing hydrothermal temperature to 220 °C led to a dramatic decrease of $k_{Cr(VI)}$ to 0.0254 min^{-1}, by which Cr (VI) was fully removed within 240 min. This might be related to that the

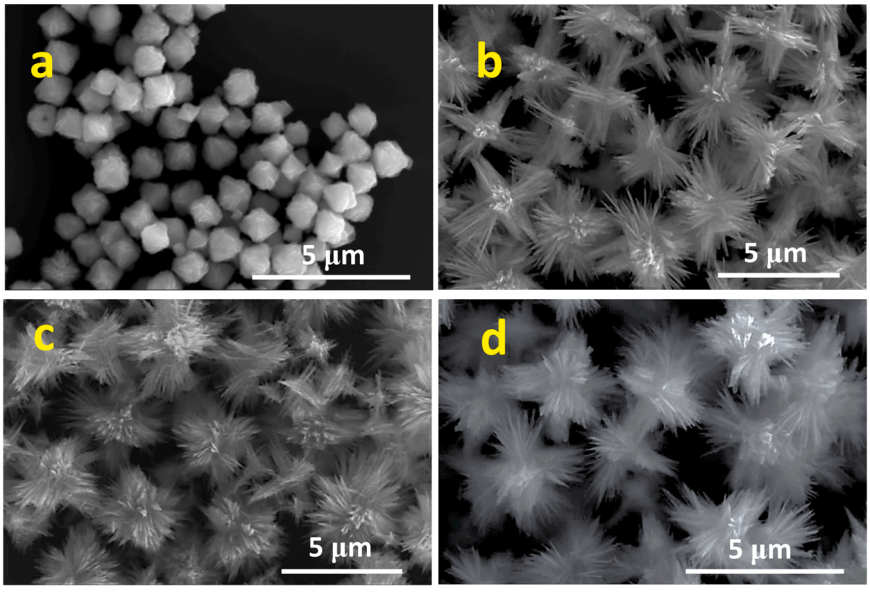

Fig. 4. FESEM images of the hexapod-like pyrite nanosheet clusters synthesized at 120 °C with different hydrothermal times in the presence of fluoride ion: (a) 1 h; (b) 2 h; (c) 4 h; (d) 24 h.

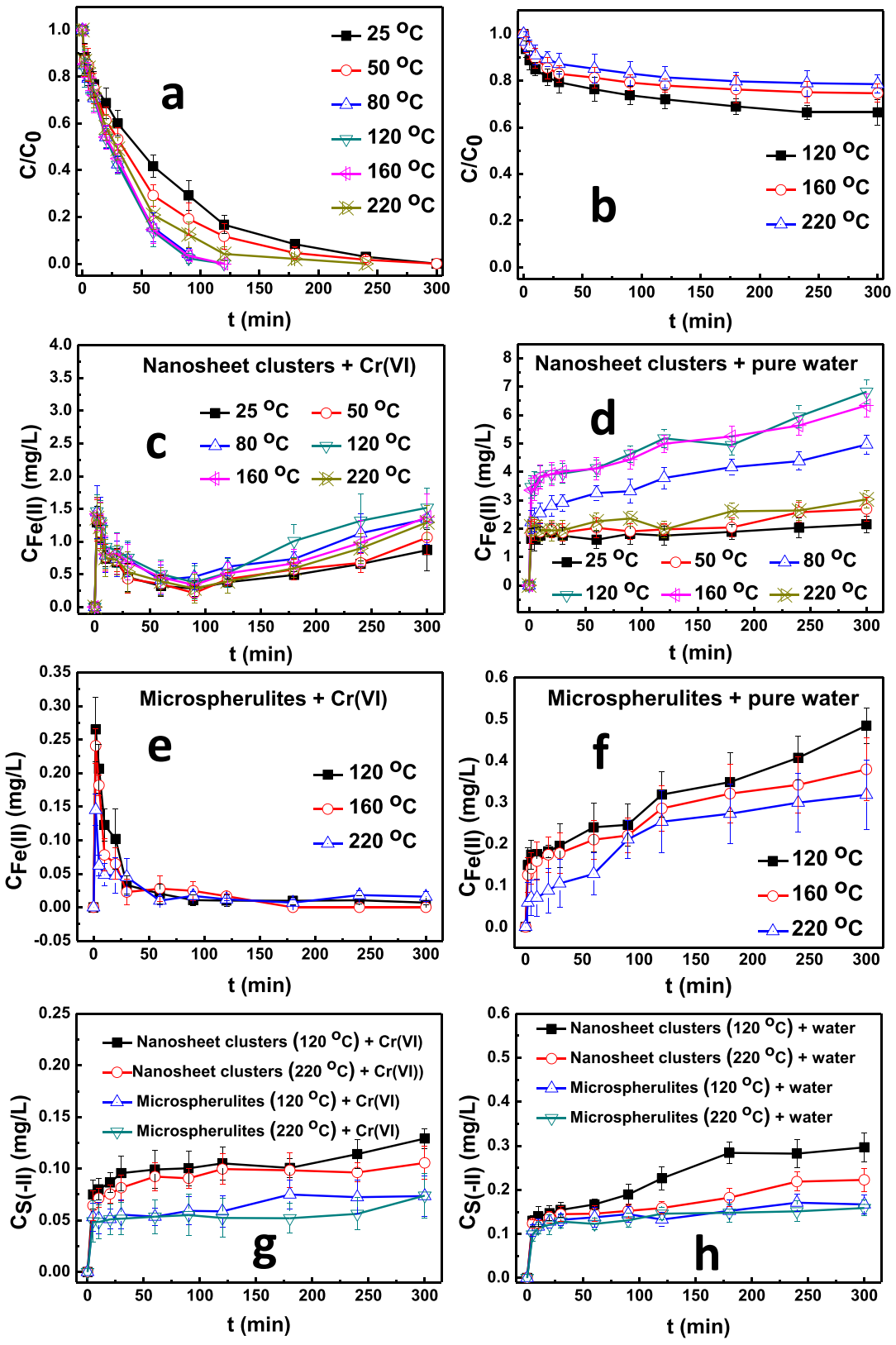

Fig. 5. Removal curves of Cr(VI) (20 ppm) from water by (a) the hexapod-like pyrite nanosheet clusters and (b) the pyrite microspherulites synthesized at different hydrothermal temperatures; The aqueous concentrations of Fe(II) in the suspensions in the presence (c) and absence (d) of Cr(VI) with the addition of the hexapod-like pyrite nanosheet clusters synthesized at different hydrothermal temperatures; The aqueous concentrations of Fe(II) in the suspensions in the presence (e) and absence (f) of Cr(VI) with the addition of the pyrite microspherulites synthesized at different hydrothermal temperatures; The aqueous concentrations of S(-II) in the suspensions in the presence (g) and absence (h) of Cr(VI) with the addition of the hexapod-like pyrite nanosheet clusters and the pyrite microspherulites synthesized at different hydrothermal temperatures.

shorten and coarsened pyrite nanosheets decreased the specific surface area of pyrite, and thereby decreased the removal rate of Cr(VI) to a certain extent. Specifically, as shown in Figs. S7, the specific surface area of the hexapod-like pyrite nanosheet clusters synthesized at 25, 50, 80, 120, 160, and 220 °C was 4.32, 4.34, 6.39, 6.63, 4.78, and 4.15 m^2/g, respectively.

Fig. 5b shows the removal of Cr(VI) by the pyrite microspherulites prepared at various hydrothermal temperatures (120–220 °C) in the absence of fluoride ion for hydrothermal reaction 24 h. The removal rate of Cr(VI) steadily decreased with increasing hydrothermal temperatures from 120 to 220 °C. However, only approximately 33.62%, 25.42%, and 21.49% of Cr(VI) was removed after 300 min by the samples prepared at 120, 160, and 220 °C, respectively. Comparatively, these pyrite microspherulites exhibited significantly lower Cr(VI) removal efficiencies than those hexapod-like pyrite nanosheet clusters prepared with the addition of fluoride ion, indicating that the hexapod-like pyrite nanosheet clusters had dramatically higher Cr(VI) removal capacities than microspherulites. This might be related to the higher specific surface area of nanosheets facilitated the removal of Cr(VI) via surface complexation, adsorption, and subsequent reduction (Tang et al., 2021). The specific surface area of the pyrite microspherulites (Figs. S7) synthesized at 120, 160, and 220 °C was 3.71, 3.22, and 2.49 m^2/g,

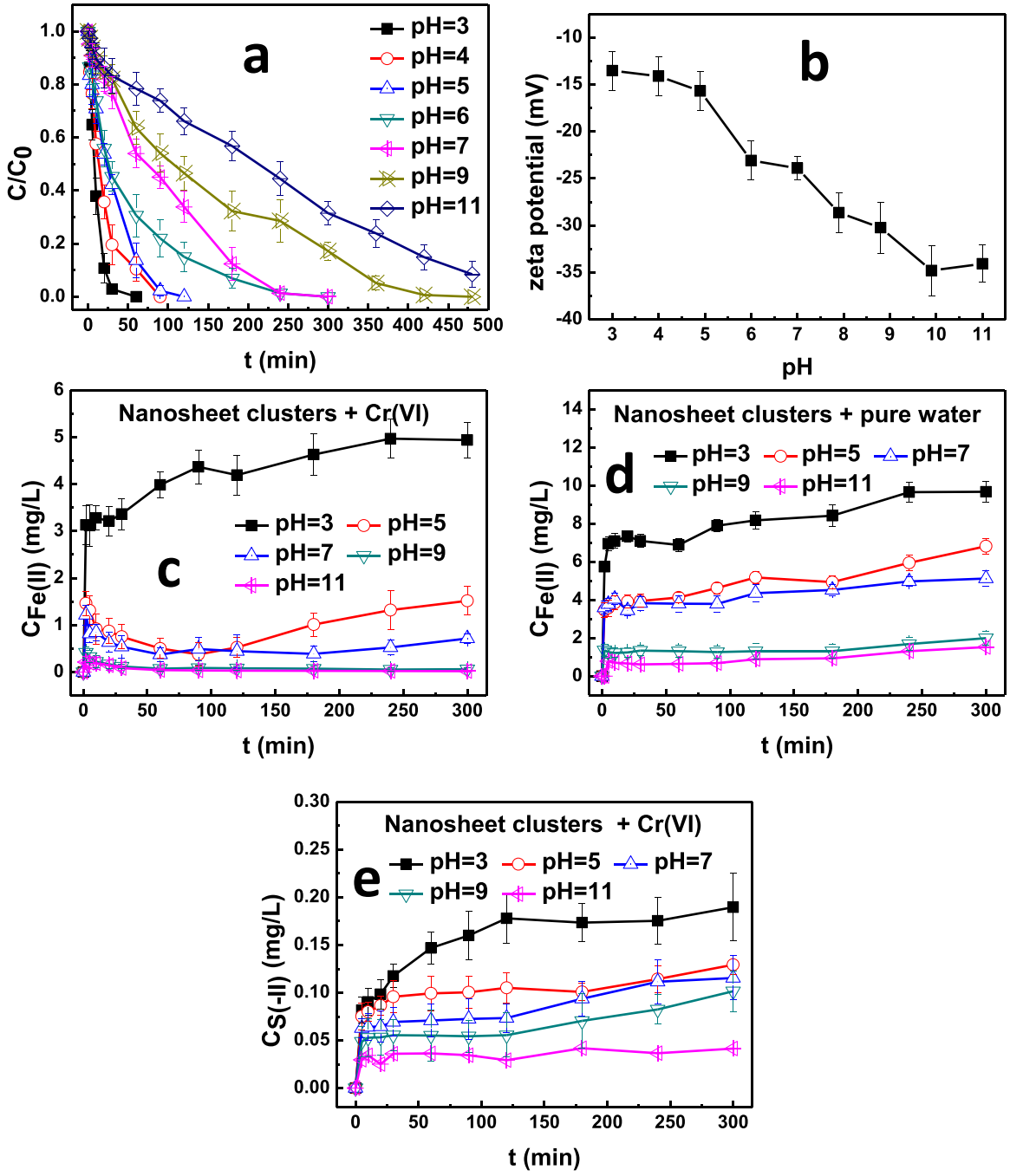

Fig. 6. (a) Removal curves of Cr(VI) from water at various pH using the optimized hexapod-like pyrite nanosheet clusters; (b) Zeta potential values of the optimized hexapod-like pyrite nanosheet clusters at different pHs; The aqueous concentrations of Fe(II) in the suspensions in the presence (c) and absence (d) of Cr(VI) with the addition of the optimized hexapod-like pyrite nanosheet clusters at different initial pHs; (e) The aqueous concentrations of S(-II) in the suspensions in the presence of Cr(VI) with the addition of the optimized hexapod-like pyrite nanosheet clusters at different initial pHs.

respectively. From the results, it can be found that the hexapod-like pyrite nanosheet clusters prepared at 120 °C possesses highest Cr(VI) removal activity. Therefore, it was employed as the optimized hexapod-like pyrite nanosheet clusters to investigate the removal of Cr (VI) in the following experiments.

However, it should be noted that the hexapod-like pyrite nanosheet clusters only had 2–3 times higher surface areas than the microspherulites, but they had significantly high performances in the Cr(VI) removal. This means that the specific surface area might be not the dominant factor controlling the Cr(VI) removal. Thus, the aqueous concentrations of Fe(II) and S(-II) as a function of stirring time for suspensions during the reaction process were measured in the presence and absence of Cr(VI) (Fig. 5c–h). Dissolved Fe(II) and S(-II) could be detected in the solution, suggesting the oxidation dissolution of pyrite surface. In the presence and absence of Cr(VI), the concentrations of dissolved Fe(II) for the hexapod-like pyrite nanosheet clusters increased initially with increasing hydrothermal temperatures from 25 to 120 °C, and then decreased with increasing hydrothermal temperatures to 220 °C. The concentrations of dissolved Fe(II) and S(-II) in the absence of Cr(VI) (pure water) were remarkable higher than the system in the presence of Cr(VI). In the presence of Cr(VI), the concentration of dissolved Fe(II) was decreased swiftly at initial 90 min, followed by a more gradual increase. This could be ascribed to the transformation of dissolved Fe(II) to Fe(III) by Cr(VI), which have lower solubility. With the reduction of Cr(VI), the concentration of dissolved Fe(II) increased gradually due to the dissolution of Fe(II) from pyrite surface. The dissolved Fe(II) concentration in the suspension is positively relevant to the removal rate of Cr(VI), indicating that Cr(VI) could be reduced to Cr(III) by dissolved Fe(II). Furthermore, the concentrations of dissolved Fe(II) for the hexapod-like pyrite nanosheet clusters were about 10 times higher than that of microspherulites, indicating that the hexapod-like pyrite nanosheet clusters have a higher release rate of Fe(II) and S(-II) due to they have more edges and corners. Therefore, more dissolved Fe(II) and S(-II) into the suspension released for nanosheet clusters should also be responsible for the enhanced removal rate of Cr(VI).

3.3. Removal of Cr(VI) by the optimized hexapod-like pyrite nanosheet clusters at different conditions

Due to the surface characteristics of solid materials and chemical speciation of Cr(VI) in aqueous solutions are dominated by solution pH value, pH value has been commonly regarded as primary environmental parameters to influence Cr(VI) removal. Apparently, the removal rate of Cr(VI) (Fig. 6a) was highly pH dependent, and the removal efficiencies steadily decreased with increasing solution initial pH from 3.0 to 11.0, indicating that acidic conditions can facilitate the Cr(VI) removal. Specifically, $k_{Cr(VI)}$ was 0.1141, 0.0537, 0.0383, 0.0170, 0.0105, 0.0061, and 0.0036 min^{-1} at initial pH 3.0, 4.0, 5.0, 6.0, 7.0 9.0, and 11.0, respectively. H^+ is needed for Cr(VI) conversion to Cr(III) ($HCrO_4^- + 7H^+ + 3Fe^{2+} \rightarrow 3Fe^{3+} + Cr^{3+} + 4H_2O$), and thus the increased H^+ concentration with lower pH can significantly promote Cr(VI) reduction to Cr(III) (Farooqi et al., 2021). Fig. 6b illustrates the zeta potential values of the optimized hexapod-like nanosheet clusters at different pHs. The zeta potential values of the as-synthesized pyrite dramatically increased in magnitude from − 13.53 mV at pH 3.0 to − 34.80 mV at pH 9.9, and then reached a relatively constant value at a solution pH over 9.9. This indicates that the surface of pyrite is negatively charged at all tested pH conditions (3.0–11.0) owing to the surface functional groups (including ≡S–H, ≡S–OH, and ≡Fe–OH) on pyrite surface are predominantly responsible for the surface charge characteristics (Nie et al., 2022). Deprotonation of these chemical functional groups would yield negatively charged surface sites (Weerasooriya and Tobschall, 2005; Bebie et al., 1998). The surface negative charge density on the pyrite surface increases with the increase of the solution pH due to a greater extent of deprotonation of surface functional groups, leading to a significant increase in the electrostatically repulsion force between pyrite and Cr(VI). Thus, the adsorption and reduction of Cr(VI) remarkably declined with rising solution pH. Under acidic condition, a higher concentration of dissolved Fe^{2+} and S^{2-} generated from the dissolution of pyrite by consuming H^+ could promote aqueous Cr(VI) reduction (Liu et al., 2019; Tang et al., 2021). Furthermore, in acidic medium (pH ≤ 6.0), the chemical species of Cr(VI) in aqueous solutions were $HCrO_4^-$, $H_2CrO_{4(aq)}$, and $Cr_2O_7^{2-}$. At pH > 6.0, CrO_4^{2-} was the dominated chemical form of Cr(VI) in water, which was more difficult to be reduced than $HCrO_4^-$, $H_2CrO_{4(aq)}$, and $Cr_2O_7^{2-}$ (Stern et al., 2021; Yao et al., 2020). Cr(VI) species can adsorb on the pyrite surface via an outer-sphere mechanism through H-bonding and ion-dipole attraction (Cr—O•••H—O—Fe), and surface complexation with a coordinatively unsaturated surface disulfide S to form Cr(VI)-thioester complexes (Gao et al., 2020; Graham and Bouwer, 2012). In addition, $HCrO_4^-$ was favorably adsorbed onto pyrite due to its low adsorption free energy compared with other chemical species of Cr(VI). The formation of Cr (III)/Fe(III) oxides/hydroxides precipitations on the surface of pyrite under alkaline condition also interfered the electron transfer between pyrite surface and Cr(VI) due to the blocking available reaction sites inhibited the adsorption as well as reduction of Cr(VI), and thus decreased the removal efficiency (Lv et al., 2019). Furthermore, the decreased Cr(VI) removal with increasing solution initial pH was also related to decreasing Fe(II) solubility. The concentrations of dissolved Fe (II) and S(-II) decreased with increasing initial pH of suspension (Fig. 6c–e), suggesting that acidic pH facilitates the dissolution of Fe(II) from pyrite. A decrease in dissolved Fe(II) and S(-II) in solution with increasing solution initial pH would decrease the reduction rate of Cr (VI) in solution. Therefore, the cumulative effects of the variation in surface characteristics of materials, the concentrations of dissolved Fe (II) and S(-II), and chemical speciation of Cr(VI) in aqueous solutions led to the remarkable decrease trend of the Cr(VI) removal rate with rising pH.

Temperature is expected to influence the removal of Cr(VI) by the hexapod-like pyrite nanosheet clusters and was thus systematically investigated (Fig. 7a). It can be seen that the removal rate of Cr(VI) increased rapidly with elevating temperature from 25 to 55 °C, and the time needed to fully remove Cr(VI) decreased from 120 to 10 min. The $k_{Cr(VI)}$ was 0.0383, 0.0536, 0.1536, 0.3284 min^{-1} with the solution temperature of 25, 35, 45, 55 °C. As the temperature further increased to 60 °C, the removal rate of Cr(VI) (with the $k_{Cr(VI)}$ of 0.3652 min^{-1}) increased slightly, and Cr(VI) could be fully removed within 10 min. This phenomenon indicates that the high temperature favored Cr(VI) removal by hexapod-like pyrite nanosheet clusters. Higher temperature could increase the Brownian motion of Cr(VI) and pyrite, and thus reinforcing the diffusion control on the adsorption as well as reduction of Cr(VI) (He et al., 2020). Moreover, increasing temperature can promote the dissolution of pyrite and subsequent reduction of Cr(VI). Fig. 7b and c show the Fe(II) concentrations in the solution at different temperatures in the presence and absence of Cr(VI). The results confirmed that increasing the temperature would significantly promote the dissolution of pyrite to release Fe(II) and S(-II) into the aqueous solution, which could accelerate the reduction of aqueous Cr(VI) to Cr (III).

3.4. Transformation products of Cr(VI)

The variations in the crystal phase composition and the surface elemental valence states information of the hexapod-like pyrite nanosheet clusters before and after the reaction with Cr(VI) (20 and 200 ppm, respectively) were distinguished via XRD and XPS, respectively. As shown in Fig. 8a, the samples after the reaction with Cr(VI) exhibited the similar diffraction peaks as freshly prepared pyrite (before the reaction with Cr(VI)), but the peak intensities were much weaker especially after reacting with high concentrations of Cr(VI). This might be ascribed to that the oxidative dissolution of pyrite surfaces after the reaction with Cr (VI) can markedly decrease the size of pyrite crystal particles. No

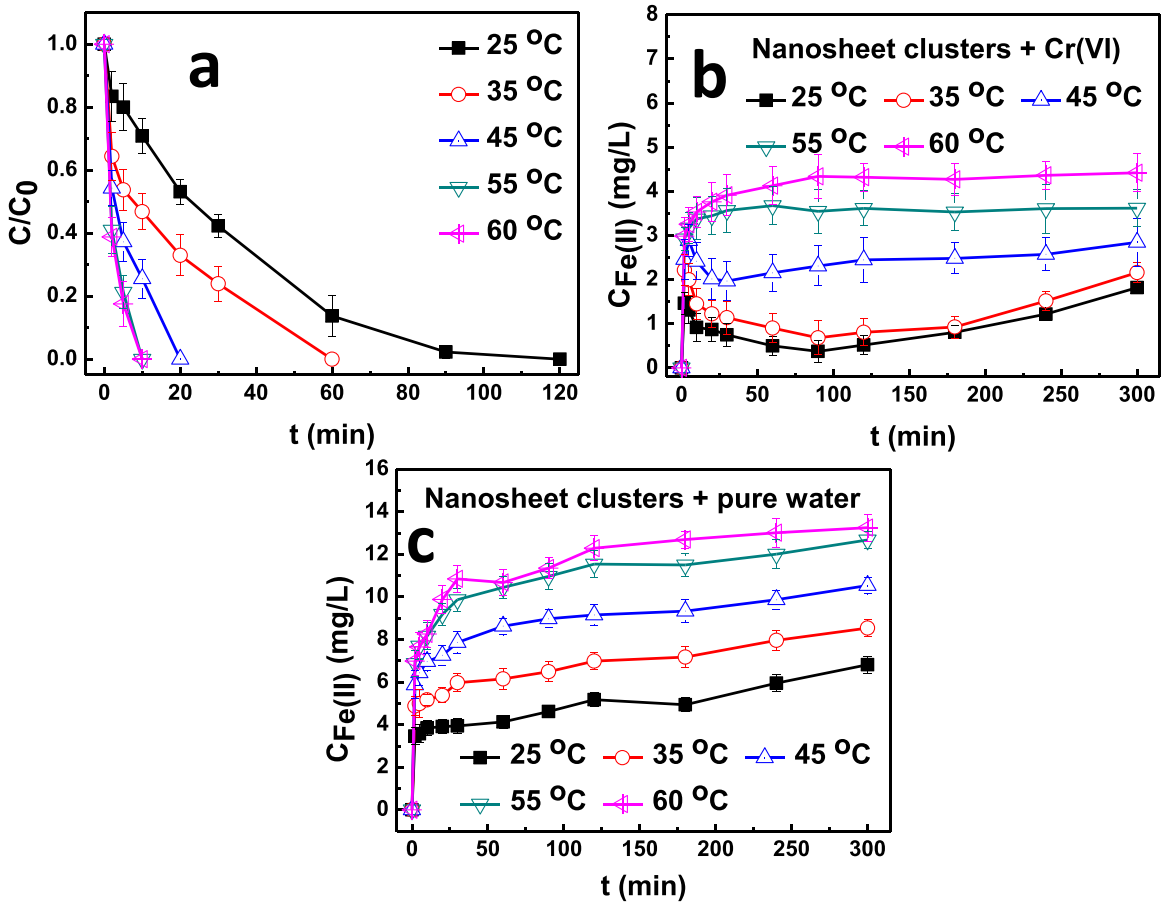

Fig. 7. (a) Removal curves of Cr(VI) from water at various temperatures; The aqueous concentrations of Fe(II) in the suspensions in the presence (b) and absence (c) of Cr(VI) with the addition of the optimized hexapod-like pyrite nanosheet clusters at different temperatures.

crystalline phase of iron (hydroxide) oxide or chromium (hydroxide) oxide was observed, suggesting the amorphous feature of these products (Lv et al., 2019).

Fig. 8b and c show that the freshly prepared pyrite is composed of the elements S and Fe, respectively. The S 2p bands for freshly prepared pyrite can be fitted with the doublets at binding energies of 162.4 eV and 163.6 eV, which corresponds to polysulfide species (S_2^{2-}) in pyrite (Mikhlin et al., 2006; Blanchard et al., 2007; Guevremont et al., 1998). After reacting with Cr(VI), two new peaks appeared at 168.5 and 169.5 eV, which can be assigned to surface-bound SO_4^{2-}, confirming that S species in solid products of the reaction between Cr(VI) and pyrite mainly existed in the form of SO_4^{2-} due to the oxidation of S_2^{2-} on pyrite surface by Cr(VI) (Wang et al., 2019a). As shown in Fig. 8c, the Fe $2p_{3/2}$ peak at 707.1 eV is unambiguously assigned to low spin bulk Fe^{2+} existed in the form of Fe(II)-S in pyrite phase. The other peak centered at 709 eV is attributed to Fe(III)-S or Fe surface state of Fe-surf. The existence of Fe(III)-S indicates that sulfur-defects exist on the pyrite surface (Zhang et al., 2016). The presence of Fe-surf. can be interpreted to be high-spin Fe^{2+} surface ions due to the coordination change of Fe from octahedral to square pyramidal yields unpaired electrons in the valence band (Liu et al., 2019; Nesbitt et al., 1998). However, after the reaction with Cr(VI), the peaks of Fe 2p spectra markedly changed compared with those before the reaction. The peak at 709 eV vanished and the intensity of the peak at 707.1 eV became significantly weaker, which is concomitant with appearance of a new peak with the binding energy of 711.1 eV corresponding to Fe $2p_{3/2}$ for Fe(III)-O in iron (hydroxide) oxides or $Fe_2(SO_4)_3$, indicating the oxidation of Fe(III)-S or Fe-surf. by Cr (VI) and the formation of a thin layer of Fe(III)-O-related products on pyrite surface (Wang et al., 2019a; Liu et al., 2011). This further confirms that FeS_2 on the surface of pyrite would be oxidized into Fe (III)-O and SO_4^{2-} in the presence of Cr(VI) due to both S_2^{2-} and Fe^{2+} participated in the chemical reaction with Cr(VI).

Fig. 8d shows that the peak of chromium species can be detected on pyrite surface after adding Cr(VI), suggesting the accumulation of Cr species on pyrite surface. Two peaks at 577.1 eV and 587.1 eV can be assigned to Cr $2p_{3/2}$ and Cr $2p_{1/2}$ binding energies of Cr(III) in $Cr(OH)_3$, respectively, indicating that most of adsorbed Cr(VI) was reduced to Cr (III) by pyrite. When the Cr(VI) concentrations increased to 200 ppm, a low level of peak at 579 eV corresponding to Cr(VI)-O can be detected on the surface of pyrite, and the relative fraction (11.6% of the total Cr peak area) of Cr(VI) was much lower than that (88.4%) of Cr(III), suggesting that reductive precipitation was the primary mechanism for Cr (VI) removal. This indicates that most of adsorbed Cr(VI) species were reduced to $Cr(OH)_3$, and Cr(III) as well as Cr(VI) species can also coexist on the surface of pyrite with addition of high concentrations of Cr(VI) (Sahu et al., 2019b, 2019a). High concentrations of Cr(VI) could also lead to the passivation of pyrite surface and subsequent decrease of available surface sites for reduction of Cr(VI). Furthermore, the peak intensity of Cr(III) increased significantly with increasing Cr(VI) concentrations, suggesting that Cr(III) should be deposited as an insoluble (hydr)oxide precipitate (such as $Cr(OH)_3$) and accumulated on the pyrite surface (Liu et al., 2011; Lu et al., 2018). Furthermore, the concentrations of Cr(VI), Cr(III), Cr_{total} in aqueous solution were also measured and the results are illustrated in Fig. 8e. The concentrations of Cr(VI) and Cr_{total} dropped with increasing reaction time, while it increased for Cr(III). After 120 min reaction, about 78% Cr_{total} was removed in aqueous solution. Combined with the XPS results, there is no doubt that the vanishment of Cr(VI) should be caused by reduction of Cr

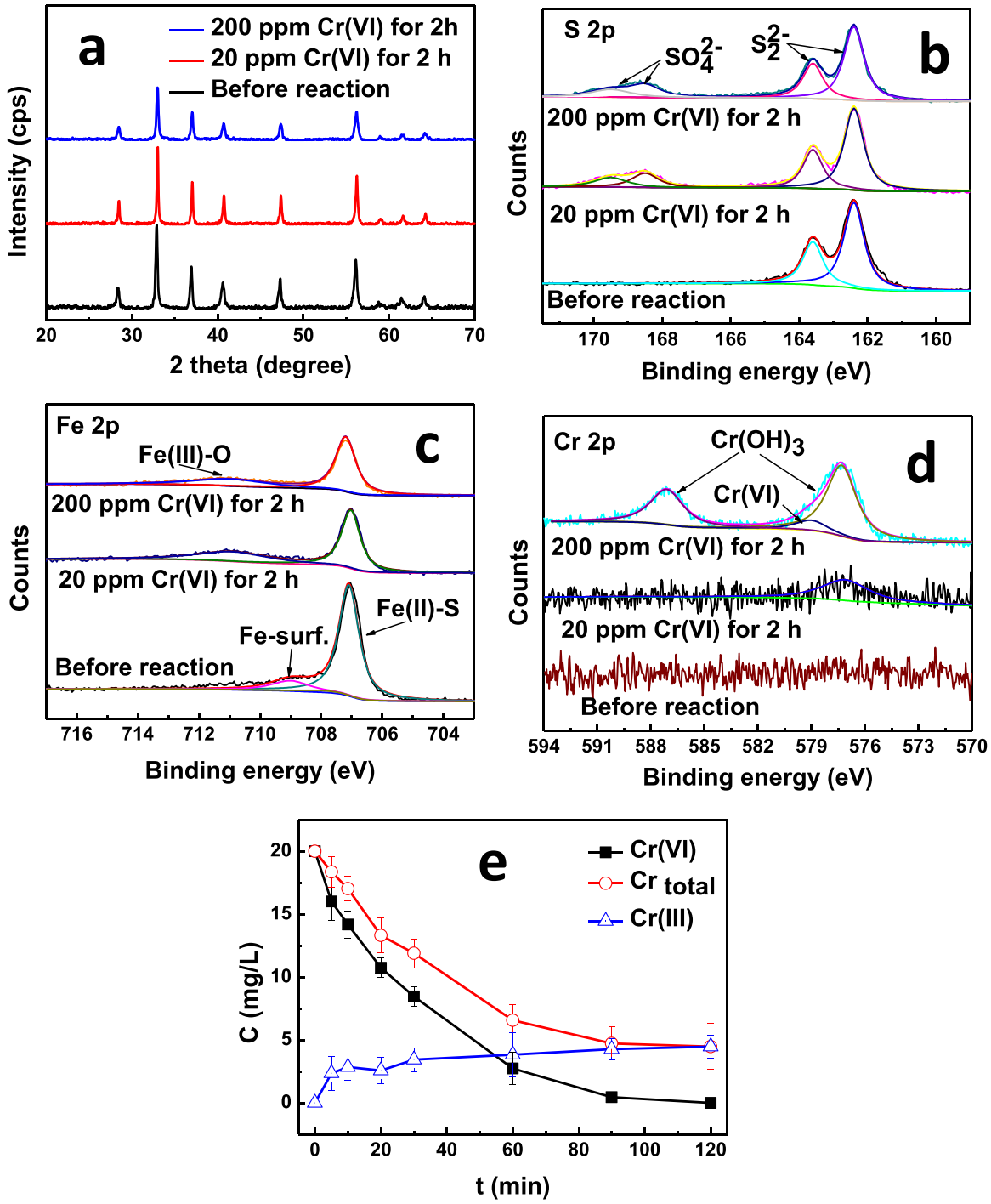

Fig. 8. XRD patterns (a), XPS spectra of S 2p (b), Fe 2p (c) and Cr 2p (d) for the optimized hexapod-like pyrite nanosheet clusters before and after reaction with Cr (VI); (e) the concentrations of Cr(VI), Cr(III), and Cr_{total} in aqueous solution during the removal process of Cr(VI) by the optimized hexapod-like pyrite nanosheets clusters with the initial pH of 5.0.

(VI) to Cr(III), and the decrease of Cr_{total} is the result of the subsequent adsorption of Cr(III) onto pyrite (Kang et al., 2020).

3.5. *Removal mechanism of Cr(VI) by the hexapod-like pyrite nanosheet clusters*

Based on the above analysis, a possible mechanism for Cr(VI) removal by the hexapod-like pyrite nanosheet clusters could be proposed and presented in Scheme 1. The rapid adsorption on the surface of pyrite followed by reduction of Cr(VI) and precipitation of Cr(III) hydroxides/oxyhydroxides were involved during the removal process of Cr(VI) (Liu et al., 2019). Cr(VI) could be adsorbed on the pyrite surface under acid condition via an outer-sphere mechanism through H-bonding and ion-dipole attraction (Cr—O•••H—O—Fe). The surface complexation with a coordinatively unsaturated surface disulfide S leads to the formation of Cr(VI)-thioester complexes, which can subsequently be reduced to Cr(III) by Fe(II) and S_2^{2-} on the pyrite surface (Gao et al., 2020). Within the initial ~20 min in the reaction progress, the sharp drop in the concentration of aqueous Cr(VI) implies that Cr(VI) was rapidly adsorbed on pyrite surface under an adsorption-limited regime.

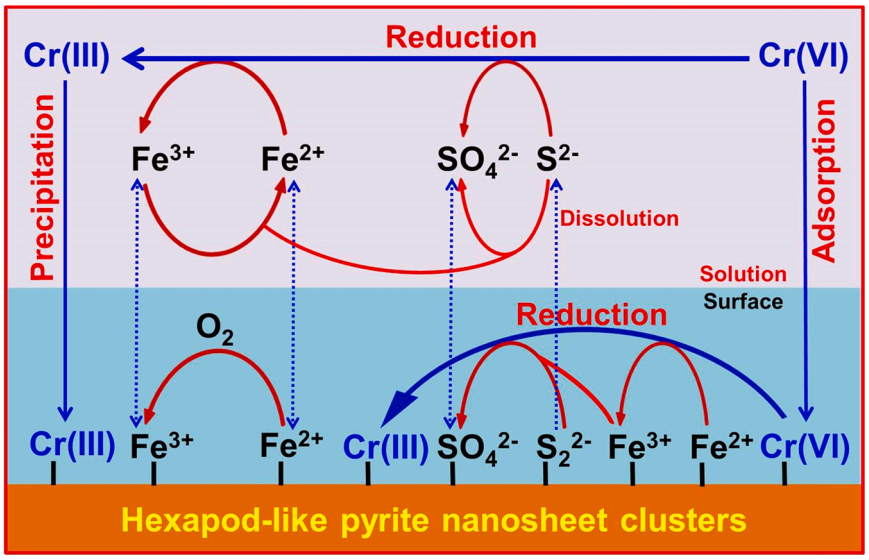

Scheme 1. Proposed mechanism for Cr(VI) removal by the hexapod-like pyrite nanosheet clusters.

The subsequent slow removal of Cr(VI) over the bulk of the time course can be ascribed to Cr(VI) removal under surface site saturation conditions (Graham and Bouwer, 2012). At the same time, the oxidation dissolution of pyrite can release Fe(II) and S(-II) into the aqueous solution, which can also reduce the aqueous Cr(VI) to Cr(III) (Wang et al., 2019b; Tang et al., 2021). Correspondingly, Fe(II), S_2^{2-} along with S(-II) are simultaneously oxidized to Fe(III) and SO_4^{2-}, respectively (Demoisson et al., 2005). The aqueous Cr(III) and Fe(III) species could be subsequently precipitated as solid phase in the form of $Cr(OH)_3$ and iron (oxy)hydroxides due to their lower solubility. These results prove that the hexapod-like pyrite nanosheet clusters not only provide the high surface area for adsorption of Cr(VI), but also act as highly reactive reducing agent to reduce adsorbed Cr(VI) as well as aqueous Cr(VI) (Farooqi et al., 2021; Wang et al., 2019a; Liu et al., 2019). Furthermore, the dissolved Fe(III) can strongly bind with the surface of pyrite and subsequently oxidize pyrite to SO_4^{2-} concomitant with the release of dissolved Fe(II), which is favorable for continuous replenishment of new surface reactive sites at the pyrite surface and the further reduction of Cr (VI). This leads to the reduction process of Cr(VI) by the hexapod-like pyrite nanosheet clusters predominantly occurring at the mineral-water interface (Graham and Bouwer, 2012). The Fe redox cycling, including the oxidation of Fe(II) and reduction of Fe(III) on the surface of pyrite, will continue until all the reactive sites on the pyrite surface are covered by $Cr(OH)_3$ and iron (oxy)hydroxides precipitation (Yang et al., 2021; Tang et al., 2021; Kantar et al., 2015). The reaction process and relative mechanism can be described as below:

$$2FeS_2 + 2H_2O + 7O_2 \rightarrow 2Fe^{2+} + 4SO_4^{2-} + 4H^+ \quad (1)$$

$$4Fe^{2+} + O_2 + 4H^+ \rightarrow 4Fe^{3+} + 2H_2O \quad (2)$$

$$HCrO_4^- + 7H^+ + 3Fe^{2+} \rightarrow 3Fe^{3+} + Cr^{3+} + 4H_2O \quad (3)$$

$$5HCrO_4^- + 19H^+ + FeS_2 \rightarrow Fe^{3+} + 5Cr^{3+} + 12H_2O + 2SO_4^{2-}. \quad (4)$$

$$FeS_2 + 14Fe^{3+} + 8H_2O \rightarrow 15Fe^{2+} + 16H^+ + 2SO_4^{2-} \quad (5)$$

$$\equiv 3Fe - S - S - (Fe(II)) + HCrO_4^- + 7H^+ \rightarrow \equiv 3Fe - S - S - (Fe(III)) + Cr^{3+} + 4H_2O \quad (6)$$

$$Cr^{3+} + 3OH^- \rightarrow Cr(OH)_3. \quad (7)$$

$$Fe^{3+} + 3OH^- \rightarrow Fe(OH)_3 \quad (8)$$

3.6. Stability and reusability of the hexapod-like pyrite nanosheet clusters for removing Cr(VI)

The changes in the hydrodynamic diameters of the hexapod-like pyrite nanosheets clusters as well as the microspherulites synthesized at different hydrothermal temperatures in the suspension during the removal process of Cr(VI), and the effect of different initial pHs on the changes in the hydrodynamic diameters of the optimized hexapod-like pyrite nanosheets clusters were measured by Dynamic light scattering (Figs. S8). Moreover, FESEM images (Figs. S9) of the optimized hexapod-like pyrite nanosheets clusters after reaction with Cr(VI) at different times were also observed. The results show that the hexapod-like pyrite nanosheets clusters did not aggregate during the reaction process. The hydrodynamic diameters and the average sizes of the hexapod-like pyrite nanosheets clusters were almost same after the removal process of Cr(VI). This indicates that the special hexapod-like morphological structure for the hexapod-like pyrite nanosheets clusters could effectively prevent the agglomeration of pyrite nanosheets clusters due to the steric hindrance and electrostatic repulsion were provided by the surface of the hexapod-like pyrite nanosheets clusters (Yao et al., 2020).

As shown in Fig. 9, after 5 recycling runs, there was no decrease in Cr (VI) removal efficiency using the optimized hexapod-like pyrite

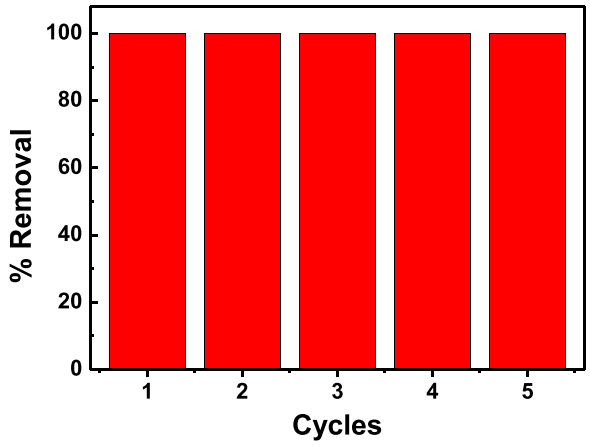

Fig. 9. Stability test of the optimized hexapod-like pyrite nanosheet clusters for the removal of Cr(VI).

nanosheet clusters, and Cr(VI) removal efficiency was still 100% after 5 cycles, indicating that the optimized hexapod-like pyrite nanosheet clusters material has high stability and longevity. Furthermore, to evaluate the safety of the hexapod-like pyrite nanosheet clusters after reaction with Cr(VI), the leaching experiment was also conducted (data not shown in here). The concentration of Cr(VI) in the solution could not be detected after one weeks, suggesting that the hexapod-like pyrite nanosheet clusters has great application potentials in purification Cr(VI) contaminated wastewater.

4. Conclusion

In summary, a novel hexapod-like pyrite nanosheet clusters material was successfully synthesized via a facile hydrothermal method with the assistance of fluorides. The fluoride ion played a crucial role in controlling crystal growth rate, morphology and size of the as-prepared pyrite. The products were pyrite microspherulites without fluoride ion. The hexapod-like pyrite nanosheet clusters had dramatically higher Cr(VI) removal efficiencies than microspherulites due to the higher specific surface area and releasing more dissolved Fe(II) and S(-II) into the suspension to reduce Cr(VI) to Cr(III). The removal efficiency of Cr (VI) decreased with increasing initial pH from 3.0 to 11.0. The removal rate of Cr(VI) increased with elevating temperature due to increasing the temperature would significantly promote the dissolution of pyrite to release Fe(II) and S(-II) into the aqueous solution to accelerate the reduction of aqueous Cr(VI) to Cr(III). The rapid adsorption on the surface of pyrite followed by the reduction of Cr(VI) and precipitation of Cr(III) hydroxides/oxyhydroxides were responsible for the removal of Cr (VI). The hexapod-like pyrite nanosheet clusters material has high stability and longevity, and Cr(VI) removal efficiency was still 100% after 5 cycles. Overall, the shape of hexapod-like nanosheet clusters can effectively prevent the aggregation of pyrite particles and enhance their size uniformity, and consequently Cr(VI) removal efficiency. Our study provides an effective and reliable technology for eliminating Cr(VI) contamination in water via simultaneous adsorption and reduction.

CRediT authorship contribution statement

Xin Nie: Methodology, Writing – original draft. **Guiying Li:** Manuscript revision. **Yun Wang**: Supervision, Writing – review & editing. **Yingmei Luo**: Data curation. **Lei Song**: Data curation. **Shuguang Yang**: Data curation. **Quan Wan**: Conceptualization, Supervision.

Declaration of Competing Interest

The authors declare that they have no known competing financial interests or personal relationships that could have appeared to influence the work reported in this paper.

Acknowledgements

This work was financially supported by the B-type Strategic Priority Program of the Chinese Academy of Sciences (XDB41000000), Guizhou Provincial Science and Technology projects ([2020]1Z039), National Natural Science Foundation of China (41902041, 41872046). The thanks also given to Hengyan Yan, Guotao Chen, Dr. Shanshan Li and Dr. Yanhui Niu for their help of data curation.

Appendix A. Supporting information

Supplementary data associated with this article can be found in the online version at doi:10.1016/j.jhazmat.2021.127504.

References

Azeez, N.A., Dash, S.S., Gummadi, S.N., Deepa, V.S., 2021. Nano-remediation of toxic heavy metal contamination: hexavalent chromium [Cr(VI)]. Chemosphere 266.
Bai, Y.X., Yeom, J., Yang, M., Cha, S.H., Sun, K., Kotov, N.A., 2013. Universal synthesis of single-phase pyrite FeS2 nanoparticles, nanowires, and nanosheets. J. Phys. Chem. C 117, 2567–2573.
Balasubramanian, S., Pugalenthi, V., 1999. Determination of total chromium in tannery waste water by inductively coupled plasma-atomic emission spectrometry, flame atomic absorption spectrometry and UV–visible spectrophotometric methods. Talanta 50, 457–467.
Bebie, J., Schoonen, M.A.A., Fuhrmann, M., Strongin, D.R., 1998. Surface charge development on transition metal sulfides: an electrokinetic study. Geochim. Cosmochim. Acta 62, 633–642.
Blanchard, M., Alfredsson, M., Brodholt, J., Wright, K., Catlow, C.R.A., 2007. Arsenic incorporation into FeS(2) pyrite and its influence on dissolution: a DFT study. Geochim. Cosmochim. Acta 71, 624–630.
Caban-Acevedo, M., Liang, D., Chew, K.S., DeGrave, J.P., Kaiser, N.S., Jin, S., 2013. Synthesis, characterization, and variable range hopping transport of pyrite (FeS2) nanorods, nanobelts, and nanoplates. ACS Nano 7, 1731–1739.
Demoisson, F., Mullet, M., Humbert, B., 2005. Pyrite oxidation by hexavalent chromium: Investigation of the chemical processes by monitoring of aqueous metal species. Environ. Sci. Technol. 39, 8747–8752.
Demoisson, F., Mullet, M., Humbert, B., 2007. Investigation of pyrite oxidation by hexavalent chromium: solution species and surface chemistry. J. Colloid Interface Sci. 316, 531–540.
Ekka, B., Dhar, G., Sahu, S., Mishra, M., Dash, P., Patel, R.K., 2021. Removal of Cr(VI) by silica-titania core-shell nanocomposites: in vivo toxicity assessment of the adsorbent by Drosophila melanogaster. Ceram. Int. 47, 19079–19089.
Farooqi, Z.H., Akram, M.W., Begum, R., Wu, W.T., Irfan, A., 2021. Inorganic nanoparticles for reduction of hexavalent chromium: physicochemical aspects. J. Hazard. Mater. 402.
Fernandez, P.M., Vinarta, S.C., Bernal, A.R., Cruz, E.L., Figueroa, L.I.C., 2018. Bioremediation strategies for chromium removal: current research, scale-up approach and future perspectives. Chemosphere 208, 139–148.
Gao, X.Y., Zhang, Y., Li, F.M., Tian, B.Y., Wang, X., Wang, Z.W., Carozza, J.C., Zhou, Z., Han, H.X., Xu, C.H., 2020. Surface modulation and chromium complexation: all-in-one solution for the Cr(VI) sequestration with bifunctional molecules. Environ. Sci. Technol. 54, 8373–8379.
Gong, Y.Y., Tang, J.C., Zhao, D.Y., 2016. Application of iron sulfide particles for groundwater and soil remediation: a review. Water Res. 89, 309–320.
Gong, Y.Y., Zhao, D.Y., Wang, Q.L., 2018. An overview of field-scale studies on remediation of soil contaminated with heavy metals and metalloids: technical progress over the last decade. Water Res. 147, 440–460.
Graham, A.M., Bouwer, E.J., 2012. Oxidative dissolution of pyrite surfaces by hexavalent chromium: surface site saturation and surface renewal. Geochim. Cosmochim. Acta 83, 379–396.
Guevremont, J.M., Bebie, J., Elsetinow, A.R., Strongin, D.R., Schoonen, M.A.A., 1998. Reactivity of the (100) plane of pyrite in oxidizing gaseous and aqueous environments: effects of surface imperfections. Environ. Sci. Technol. 32, 3743–3748.
He, X.Y., Min, X.B., Peng, T.Y., Zhao, F.P., Ke, Y., Wang, Y.Y., Jiang, G.H., Xu, Q.J., Wang, J.W., 2020. Mechanochemically activated microsized zero-valent iron/pyrite composite for effective hexavalent chromium sequestration in aqueous solution. J. Chem. Eng. Data 65, 1936–1945.
He, P., Zhu, J.Y., Chen, Y.Z., Chen, F., Zhu, J.L., Liu, M.F., Zhang, K., Gan, M., 2021. Pyrite-activated persulfate for simultaneous 2,4-DCP oxidation and Cr(VI) reduction. Chem. Eng. J. 406.
Hu, Y., Zheng, Z., Jia, H.M., Tang, Y.W., Zhang, L.Z., 2008. Selective synthesis of FeS and FeS2 nanosheet films on iron substrates as novel photocathodes for tandem dye-sensitized solar cells. J. Phys. Chem. C 112, 13037–13042.
Kang, L., Yang, H.P., Wang, L.N., Chai, S.Q., Zhang, R.C., Wu, J.M., Liu, X.N., 2020. Facile integration of FeS and titanate nanotubes for efficient removal of total Cr from aqueous solution: synergy in simultaneous reduction of Cr(VI) and adsorption of Cr (III). J. Hazard. Mater. 398.
Kantar, C., Ari, C., Keskin, S., 2015. Comparison of different chelating agents to enhance reductive Cr(VI) removal by pyrite treatment procedure. Water Res. 76, 66–75.
Kaur, H., Tian, R.Y., Roy, A., McCrystall, M., Horvath, D.V., Onrubia, G.L., Smith, R., Ruether, M., Griffin, A., Backes, C., Nicolosi, V., Coleman, J.N., 2020. Production of Quasi-2D platelets of nonlayered iron pyrite (FeS2) by liquid-phase exfoliation for high performance battery electrodes. ACS Nano 14, 13418–13432.
Khalid, S., Ahmed, E., Khan, Y., Riaz, K.N., Malik, M.A., 2018. Nanocrystalline pyrite for photovoltaic applications. Chemistryselect 3, 6488–6524.
Kirkeminde, A., Ren, S.Q., 2013. Thermodynamic control of iron pyrite nanocrystal synthesis with high photoactivity and stability. J. Mater. Chem. A 1, 49–54.
Kirkeminde, A., Ruzicka, B.A., Wang, R., Puna, S., Zhao, H., Ren, S.Q., 2012. Synthesis and optoelectronic properties of two-dimensional FeS2 nanoplates. ACS Appl. Mater. Interfaces 4, 1174–1177.
Liu, W., Jin, L.D., Xu, J., Liu, J., Li, Y.Y., Zhou, P.P., Wang, C.C., Dahlgren, R.A., Wang, X. D., 2019. Insight into pH dependent Cr(VI) removal with magnetic Fe_3S_4. Chem. Eng. J. 359, 564–571.
Liu, W., Wang, Y.Y., Ai, Z.H., Zhang, L.Z., 2015. Hydrothermal synthesis of FeS2 as a high-efficiency fenton reagent to degrade alachlor via superoxide-mediated Fe(II)/Fe (III) cycle. ACS Appl. Mater. Interfaces 7, 28534–28544.

Liu, G., Yu, J.C., Lu, G.Q., Cheng, H.M., 2011. Crystal facet engineering of semiconductor photocatalysts: motivations, advances and unique properties. Chem. Commun. 47, 6763–6783.

Li, T.T., Liu, H.W., Wu, Z.N., Liu, Y., Guo, Z.X., Zhang, H., 2016a. Seeded preparation of ultrathin FeS2 nanosheets from Fe_3O_4 nanoparticles. Nanoscale 8, 11792–11796.

Li, G.Y., Nie, X., Chen, J.Y., Wong, P.K., An, T.C., Yamashita, H., Zhao, H.J., 2016b. Enhanced simultaneous PEC eradication of bacteria and antibiotics by facilely fabricated high-activity {001} facets TiO_2 mounted onto TiO_2 nanotubular photoanode. Water Res. 101, 597–605.

Lu, Y., Li, Z.F., Li, J.F., Chen, K., Dong, H.P., Shou, J.X., Li, Y.M., 2018. Synergetic effect of pyrite on Cr(VI) removal by zero valent iron in column experiments: an investigation of mechanisms. Chem. Eng. J. 349, 522–529.

Lv, D., Zhou, J.S., Cao, Z., Xu, J., Liu, Y.L., Li, Y.Z., Yang, K.L., Lou, Z.M., Lou, L.P., Xu, X. H., 2019. Mechanism and influence factors of chromium(VI) removal by sulfide-modified nanoscale zerovalent iron. Chemosphere 224, 306–315.

Marinho, B.A., Cristovao, R.O., Boaventura, R.A.R., Vilar, V.J.P., 2019. As(III) and Cr(VI) oxyanion removal from water by advanced oxidation/reduction processesa review. Environ. Sci. Pollut. Res. 26, 2203–2227.

Meng, M., Wu, X.L., Zhu, X.B., Yang, L., Gan, Z.X., Zhu, X.S., Liu, L.Z., Chu, P.K., 2014. Cubic In_2O_3 microparticles for efficient photoelectrochemical oxygen evolution. J. Phys. Chem. Lett. 5, 4298–4304.

Mikhlin, Y.L., Romanchenko, A.S., Asanov, I.P., 2006. Oxidation of arsenopyrite and deposition of gold on the oxidized surfaces: a scanning probe microscopy, tunneling spectroscopy and XPS study. Geochim. Cosmochim. Acta 70, 4874–4888.

Nesbitt, H.W., Bancroft, G.M., Pratt, A.R., Scaini, M.J., 1998. Sulfur and iron surface states on fractured pyrite surfaces. Am. Miner. 83, 1067–1076.

Nie, X., Li, G.Y., Li, S.S., Luo, Y.M., Luo, W.M., Wan, Q., An, T.C., 2022. Highly efficient adsorption and catalytic degradation of ciprofloxacin by a novel heterogeneous Fenton catalyst of hexapod-like pyrite nanosheets mineral clusters. Appl. Catal. B Environ. 300, 120734.

Nie, X., Luo, S.X., Yang, M.Z., Zeng, P., Qin, Z.H., Yu, W.B., Wan, Q., 2019. Facile hydrothermal synthesis of nanocubic pyrite crystals using greigite Fe_3S_4 and thiourea as precursors. Minerals 9.

Sahu, S., Bishoyi, N., Patel, R.K., 2021a. Cerium phosphate polypyrrole flower like nanocomposite: a recyclable adsorbent for removal of Cr(VI) by adsorption combined with in-situ chemical reduction. J. Ind. Eng. Chem. 99, 55–67.

Sahu, S., Bishoyi, N., Sahu, M.K., Patel, R.K., 2021b. Investigating the selectivity and interference behavior for detoxification of Cr(VI) using lanthanum phosphate polyaniline nanocomposite via adsorption-reduction mechanism. Chemosphere 278.

Sahu, S., Kar, P., Bishoyi, N., Mallik, L., Patel, R.K., 2019a. Synthesis of polypyrrole-modified layered double hydroxides for efficient removal of Cr(VI). J. Chem. Eng. Data 64, 4357–4368.

Sahu, S., Mallik, L., Pahi, S., Barik, B., Sahu, U.K., Sillanpaa, M., Patel, R.K., 2020. Facile synthesis of poly o-toluidine modified lanthanum phosphate nanocomposite as a superior adsorbent for selective fluoride removal: a mechanistic and kinetic study. Chemosphere 252.

Sahu, S., Sahu, U.K., Patel, R.K., 2019b. Modified thorium oxide polyaniline core-shell nanocomposite and its application for the efficient removal of Cr(VI). J. Chem. Eng. Data 64, 1294–1304.

Shahid, M., Shamshad, S., Rafiq, M., Khalid, S., Bibi, I., Niazi, N.K., Dumat, C., Rashid, M. I., 2017. Chromium speciation, bioavailability, uptake, toxicity and detoxification in soil-plant system: a review. Chemosphere 178, 513–533.

Shao, Q.Q., Xu, C.H., Wang, Y.H., Huang, S.S., Zhang, B.L., Huang, L.H., Fan, D.M., Tratnyek, P.G., 2018. Dynamic interactions between sulfidated zerovalent iron and dissolved oxygen: mechanistic insights for enhanced chromate removal. Water Res. 135, 322–330.

Shukla, S., Xing, G.C., Ge, H., Prabhakar, R.R., Mathew, S., Su, Z.H., Nalla, V., Venkatesan, T., Mathews, N., Sritharan, T., Sum, T.C., Xiong, Q.H., 2016. Origin of photocarrier losses in iron pyrite (FeS2) nanocubes. ACS Nano 10, 4431–4440.

Stern, C.M., Jegede, T.O., Hulse, V.A., Elgrishi, N., 2021. Electrochemical reduction of Cr (vi) in water: lessons learned from fundamental studies and applications. Chem. Soc. Rev. 50, 1642–1667.

Tang, J.C., Zhao, B.B., Lyu, H.H., Li, D., 2021. Development of a novel pyrite/biochar composite (BM-FeS2@BC) by ball milling for aqueous Cr(VI) removal and its mechanisms. J. Hazard. Mater. 413.

Tripathy, S., Sahu, S., Patel, R.K., Panda, R.B., Kar, P.K., 2021. Efficient removal of Cr(VI) by polyaniline modified biochar from date (Phoenix dactylifera) seed. Groundw. Sustain. Dev. 15, 100653.

Veerakumar, P., Lin, K.C., 2020. An overview of palladium supported on carbon-based materials: synthesis, characterization, and its catalytic activity for reduction of hexavalent chromium. Chemosphere 253.

Wang, T., Liu, Y.Y., Wang, J.J., Wang, X.Z., Liu, B., Wang, Y.X., 2019a. In-situ remediation of hexavalent chromium contaminated groundwater and saturated soil using stabilized iron sulfide nanoparticles. J. Environ. Manag. 231, 679–686.

Wang, S.C., Liu, G., Wang, L.Z., 2019c. Crystal facet engineering of photoelectrodes for photoelectrochemical water splitting. Chem. Rev. 119, 5192–5247.

Wang, T., Qian, T.W., Huo, L.J., Li, Y.F., Zhao, D.Y., 2019b. Immobilization of hexavalent chromium in soil and groundwater using synthetic pyrite particles. Environ. Pollut. 255.

Weerasooriya, R., Tobschall, H.J., 2005. Pyrite-water interactions: effects of pH and pFe on surface charge. Colloid Surf. A 264, 68–74.

Wen, J., Fang, Y., Zeng, G.M., 2018. Progress and prospect of adsorptive removal of heavy metal ions from aqueous solution using metal-organic frameworks: a review of studies from the last decade. Chemosphere 201, 627–643.

Wu, Y., Wang, Y.Y., Shao, S.Q., Ma, Y.M., Zhang, J.J., Kang, W.P., Xu, J., 2020. Transformation of two-dimensional iron sulfide nanosheets from FeS2 to FeS as high-rate anodes for pseudocapacitive sodium storage. ACS Appl. Energ. Mater. 3, 12672–12681.

Xian, H.Y., Zhu, J.X., Liang, X.L., He, H.P., 2016. Morphology controllable syntheses of micro- and nano-iron pyrite mono- and poly-crystals: a review. RSC Adv. 6, 31988–31999.

Xia, S.P., Song, Z.L., Jeyakumar, P., Shaheen, S.M., Rinklebe, J., Ok, Y.S., Bolan, N., Wang, H.L., 2019. A critical review on bioremediation technologies for Cr(VI)-contaminated soils and wastewater. Crit. Rev. Environ. Sci. Technol. 49, 1027–1078.

Xu, Y.L., Chen, J.Y., Chen, R., Yu, P.L., Guo, S., Wang, X.F., 2019. Adsorption and reduction of chromium(VI) from aqueous solution using polypyrrole/calcium rectorite composite adsorbent. Water Res. 160, 148–157.

Yang, T., Gordon, Z.D., Chan, C.K., 2013. Synthesis of hyperbranched perovskite nanostructures. Cryst. Growth Des. 13, 3901–3907.

Yang, Z.H., Zhang, X.M., Jiang, Z., Li, Q., Huang, P.C., Zheng, C.J., Liao, Q., Yang, W.C., 2021. Reductive materials for remediation of hexavalent chromium contaminated soil - a review. Sci. Total Environ. 773.

Yao, Y.R., Mi, N., He, C., Zhang, Y., Yin, L., Li, J., Wang, W., Yang, S.G., He, H., Li, S.Y., Ni, L.X., 2020. A novel colloid composited with polyacrylate and nano ferrous sulfide and its efficiency and mechanism of removal of Cr(VI) from water. J. Hazard. Mater. 399.

Yasir, M.W., Siddique, M., Shabbir, Z., Ullah, H., Shah, A.A., 2021. Biotreatment potential of Co-contaminants hexavalent chromium and polychlorinated biphenyls in industrial wastewater: individual and simultaneous prospects. Sci. Total Environ., 146345

Yu, B.B., Zhang, X., Jiang, Y., Liu, J., Gu, L., Hu, J.S., Wan, L.J., 2015. Solvent-induced oriented attachment growth of air-stable phase pure pyrite FeS2 nanocrystals. J. Am. Chem. Soc. 137, 2211–2214.

Zhang, P., Yuan, S.H., Liao, P., 2016. Mechanisms of hydroxyl radical production from abiotic oxidation of pyrite under acidic conditions. Geochim. Cosmochim. Acta 172, 444–457.

Zhu, L., Richardson, B., Tanumihardja, J., Yu, Q.M., 2012. Controlling morphology and phase of pyrite FeS2 hierarchical particles via the combination of structure-direction and chelating agents. Crystengcomm 14, 4188–4195.